

Magnetization-Induced Phase Transitions on the surface of 3D Topological Insulators

Yu-Hao Wan¹ and Qing-Feng Sun^{1,2,*}

¹International Center for Quantum Materials, School of Physics, Peking University, Beijing 100871, China

²Hefei National Laboratory, Hefei 230088, China

From the low-energy model, the topological field theory indicates that the surface magnetization can open a surface gap in 3D topological insulators (TIs), resulting in a half-quantized Hall conductance. Here by employing the realistic lattice model, we show the occurrence of the surface phase transitions, accompanied with the sharp changes of the surface Chern number from $\frac{1}{2}$ to $-\frac{3}{2}$ finally to $-\frac{1}{2}$, in 3D TIs induced by surface magnetization. These surface phase transitions lead to the sudden jumps in the magneto-electric coefficient and the quantum Hall conductance, which are experimentally observable. Furthermore, we present the phase diagram that elucidates the behavior of the 3D TI surface Chern numbers under surface magnetization for different Z_4 topological numbers. Our study highlights the presence of the new phases with broken bulk-boundary correspondence and enriches understandings of the properties of TIs.

I. INTRODUCTION

Three-dimensional (3D) topological insulators (TIs), featured by a bulk band gap and gapless helical surface states protected by the time-reversal symmetry (TRS), have received intense research over the past decade [1–5]. The physics origin of the gapless surface states is well known as bulk-boundary correspondence, in which the gapless surface states are determined by the topology of the bulk band. When the TRS is broken on the surface (e.g. by the magnetization), the fall of the bulk-boundary correspondence will result in a gapped surface. Nevertheless, even if on the TRS-breaking surface, information about the bulk’s topological properties can still be manifested at the gapped surface. For instance, half-quantized anomalous Hall conductance(AHC) and topological magneto-electric (ME) effects [6, 7] can arise within the gap of the TRS-breaking surface [8–14], which relates with the topological θ -axion term in the bulk [15]. In 3D TIs, the θ -term is directly associated with the Z_2 topological index, where $\theta = \pi \pmod{2\pi}$ corresponds to a nontrivial bulk [12]. It is worth noting that the bulk-boundary correspondence on the TRS-breaking surface, and then the half-quantized AHC and the topological ME effect, are considered outcomes of low-energy models near Γ point based on topological field theory [12, 16]. For a strong magnetization with the TRS strongly broken, the availability of low-energy models is poorly studied. In reality, the system should be described on a complete Brillouin zone. The low-energy model fails to capture information from the Brillouin zone, thereby missing certain physics phenomena related to it.

In this paper, we systematically investigate the influence of surface magnetization on 3D TIs within the realistic lattice model. We discover that the increasing magnetization leads to a series of topological phase transitions on the surface of the 3D TI. Specifically, the surface Chern number transitions from $\frac{1}{2}$ to $-\frac{3}{2}$ and eventually reaches $-\frac{1}{2}$ [see Fig. 1(b)]. To quantitatively characterize these transitions, we employ a slab model and an effective three-layer model, calculating the local Chern markers from both numerical and analytical per-

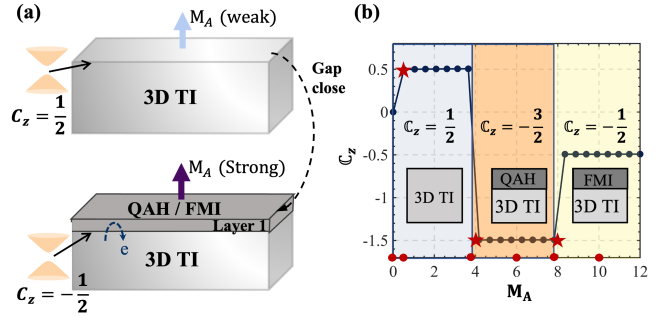


Figure 1. (a) Upper and lower parts are schematic diagrams for the surface phase of 3D TI under the weaker and stronger surface magnetization, respectively. (b) Surface Chern number C_z as a function of surface magnetization M_A . The blue, orange, and yellow regions correspond to $C_z = \frac{1}{2}$, $-\frac{3}{2}$, and $-\frac{1}{2}$. The insets illustrate schematic diagrams of the systems in the three regions.

spectives. The computational results reveal that surface magnetization initiates a non-adiabatic transformation in the first layer of the 3D TI, converting the massive Dirac fermion into a state of quantum anomalous Hall/ferromagnetic insulator (QAH/FMI). Furthermore, as the first-layer topological transition occurs, an opposing massive Dirac fermion reemerges in the second layer and results in $-\frac{1}{2}$ Chern number [see Fig. 1(a)]. Moreover, these topological phase transitions also lead to the sharp changes of both topological ME coefficient and the surface Hall conductance plateau.

The organization of this paper is as follows. In Sec. II, we present our lattice model and numerically investigate the variation of the surface Chern number with the increase of surface magnetization using a 20-layer 3D TI slab model. In Sec. III, we establish an effective 3-layer model to describe the behavior of 3D TI surface states in the presence of surface magnetization. In Sec. IV, we present a phase diagram that illustrates how different bulk topological mass terms affect the surface topological transitions induced by surface magnetization. Both the topological ME coefficient and the surface quantum Hall conductance plateaus induced by the surface topological transitions are studied in Sec. V. We discuss experimental implementation in Sec. VI and conclude with a summary. Additional computational details and supplementary figures can

* Corresponding author: sunqf@pku.edu.cn.

be found in Appendices A to E.

II. SURFACE MAGNETIZATION-INDUCED PHASE TRANSITIONS

We start with the Hamiltonian of a 3D TI in cubic lattice:

$$\mathcal{H}_{\text{TI}} = (m - 6B)s_0\sigma_z + \sum_i (2Bs_0\sigma_z \cos k_i + As_i\sigma_x \sin k_i) \quad (1)$$

where m , B and A are the model's parameters and k_i is the momentum with $i = x, y, z$. s_i and σ_i are the Pauli matrices on the spin and orbital spaces. The system exhibits a non-trivial topological phase when satisfying $0 < m < 4B$ or $8B < m < 12B$ [17]. Below, we choose $m = 2$, $B = 1$ and $A = 1$ to position the system in the nontrivial topological phase, unless mentioned otherwise. We construct a 20-layer thick slab model [Fig. 2(a)]. For the convenient observation of the influence of surface magnetization on energy bands, we introduce symmetrical magnetization on both the top and bottom surfaces, thereby opening magnetic energy gaps on both surfaces. The Hamiltonian is represented as follows:

$$H_{\text{slab}} = \begin{pmatrix} H_{lay_1} & D & 0 & \dots & 0 \\ D^\dagger & H_{lay_2} & D & \dots & 0 \\ 0 & D^\dagger & H_{lay_3} & \dots & 0 \\ \dots & \dots & \dots & \dots & \dots \\ 0 & 0 & 0 & \dots & H_{lay_{20}} \end{pmatrix}$$

The Hamiltonian for each layer is given by $H_{lay_l} = H_{lay} + \delta_{l,1}M_A s_z - \delta_{l,20}M_A s_z$ with $H_{lay} = A\sigma_x s_x \sin k_x + A\sigma_x s_y \sin k_y + [m - 6B + 2B(\cos k_x + \cos k_y)]\sigma_z s_0$. The interlayer hopping is given by $D = \frac{A}{2i}\sigma_x s_x + B\sigma_z s_0$. M_A represents the magnetization strength of the top and bottom surfaces, which can be introduced experimentally through magnetic doping or heterostructure approaches [9, 18–20].

Then we investigate the local Chern markers within the slab model to characterize the contributions of different layers to the total Chern number [21–23]. The local Chern marker projected onto layer l , denoted as $C_z(l)$, can be calculated from the expression [23]:

$$C_z(l) = \frac{-4\pi}{\mathcal{A}} \text{Im} \frac{1}{N_k} \sum_k \sum_{vv'c} X_{vck} Y_{v'ck}^\dagger \rho_{vv'k}(l) \quad (2)$$

The matrix element for the position operator along the x or y directions, is denoted as $X(Y)_{vck} = \langle \psi_{vck} | x(y) | \psi_{ck} \rangle = \frac{\langle \psi_{vck} | i\hbar v_x(v_y) | \psi_{ck} \rangle}{E_{ck} - E_{vck}}$, which is related to the energy difference between the conduction and valence bands $E_{ck} - E_{vck}$. The indices v and c represent the valence and conduction bands. $\rho_{vv'k}(l)$ is the projection matrix on to the corresponding layer l which implies a summation over all orbitals v, v', c belonging to that layer. N_k represents the number of k -points and \mathcal{A} represents the unit cell area.

In Fig. 2(b) and (c-e), we have computed the local Chern markers and corresponding band structures under some representative magnetizations, which are marked with red pentagrams in Fig. 1(b). Due to the opposite magnetization on the

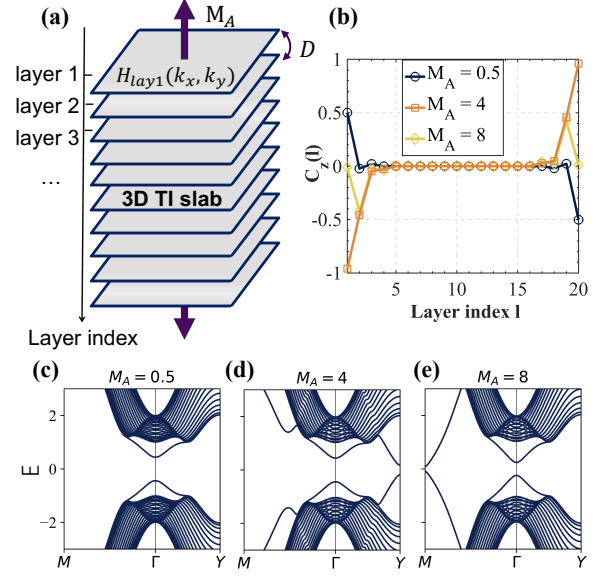


Figure 2. (a) Schematic diagram of a 20-layer slab model of a 3D TI, with opposite magnetization M_A applied to the upper and lower surfaces. D denotes inter-layer hopping. (b) Layer-resolved local Chern markers $C_z(l)$ of a 20-layer 3D TI slab model with different M_A indicated by pentagrams in Fig. 1(b). (c) Band structures under different M_A .

top and bottom surfaces, the local Chern marker on these surfaces is also opposite (see Fig. 2(b)). As a result, the overall Chern number of the system is zero, leading to the absence of a net Hall effect. However, in practical scenarios, introducing surface magnetization on only one layer can generate a net Hall effect. Subsequently, our analysis is confined to the upper half of the system due to its symmetry. The surface Chern number \mathbb{C}_z is determined by the sum of the local Chern markers $C_z(l)$ of the first several layers [23, 24]. Computational results indicate that $C_z(l)$ becomes nearly zero for $l > 4$. Therefore, we consider $\mathbb{C}_z = \sum_{l=1}^4 C_z(l)$ which is shown in Fig. 1(b). For a small magnetization M_A (e.g. $M_A = 0.5$), a gapped Dirac cone occurs at the Γ point [as shown in Fig. 2(c)], leading to the local Chern markers $C_z(1) \approx 1/2$, $C_z(20 > l > 1) \approx 0$, and the surface Chern number $\mathbb{C}_z = 1/2$ [See Figs. 2(b) and 1(b)]. This finding is well consistent with the results of previous theoretical works from the low-energy models and has been observed in the experiments [8–14]. With the increase of the surface magnetization M_A , at M_A slightly less than 4, the bands close and reopen at the X and Y points [Fig. 2(d)], leading to the local Chern marker $C_z(1)$ on the first layer abruptly jumping to -1 . Meanwhile, $C_z(2)$ of the second layer sharply changes to $-1/2$ [see the orange line in Fig. 2(b)], resulting in the surface Chern number $\mathbb{C}_z = -3/2$ [Fig. 1(b)]. With $M_A = 8$, after the bands close and reopen at the M point [Fig. 2(e)], $C_z(1)$ abruptly becomes 0, while $C_z(2)$ remains approximately $-1/2$. Consequently, $\mathbb{C}_z = -1/2$ [Fig. 1(b)]. Fig. 2(c-e) only presents several instances under distinct magnetization M_A , while a more comprehensive evolution of band

structure is documented in the Fig. 6 of Appendix A.

In the following, we will provide a physics interpretation of the transition of surface Chern number \mathbb{C}_z from $\frac{1}{2}$ to $-\frac{3}{2}$ to $-\frac{1}{2}$. When the surface magnetization M_A is relatively small, without gap closing, adiabatic changes ensure that \mathbb{C}_z remains at $\frac{1}{2}$ without alteration, which is consistent with the low-energy models [12, 13]. With the increasing of M_A , accompanied by the gap closing and reopening at points X and Y, the first layer enters the QAH phase. Simultaneously, a massive Dirac fermion reemerges in the second layer. This effect is analogous to the impact of Anderson disorders on the surface of 3D TIs [25], where the transition of the surface QAH phase also leads to the revival of topological surface states in the second layer. However, due to the effective magnetization on the second layer through second-order effects being opposite in direction to the first layer (see Appendix B), this results in a $-\frac{1}{2}$ surface Chern number on the second layer [as shown in the lower part of Fig. 1(a)]. The system can be effectively modeled as a combination of a 3D TI and a monolayer QAH system [see the inset in Fig. 1(b) or the lower part in Fig. 1(a)], leading to $\mathbb{C}_z = -1 + (-\frac{1}{2}) = -\frac{3}{2}$. As M_A continues to increase, similarly, the gap closing and reopening at point M corresponds to the transition of the first layer from the QAH phase to the FMI phase, characterized by a local Chern marker of zero. Consequently, due to the co-existence of massive Dirac fermions and FMI monolayer [the inset in Fig. 1(b)], the surface Chern number \mathbb{C}_z becomes $0 + (-\frac{1}{2}) = -\frac{1}{2}$. Additionally, it's worth mentioning that the essence of surface phase transition lies in the finite size of the Brillouin zone in real systems. Therefore, the occurrence of the phase transition is independent of the specific lattice model.

III. THREE LAYERS EFFECTIVE MODEL AND PHASE DIAGRAM

To capture the surface physics of a 3D TI in the presence of surface magnetization M_A , we employ a simplified three-layer effective model, as illustrated in Fig. 3(a). The corresponding Hamiltonian is expressed as follows:

$$H = \begin{pmatrix} H_{lay1} + M_A s_z & D & 0 \\ D^\dagger & H_{lay2} & D \\ 0 & D^\dagger & H_{lay3} + \Sigma(\varepsilon) \end{pmatrix}$$

Here the surface magnetization $M_A s_z$ is introduced in the first layer, and the bulk's effective influence is incorporated into the third layer through a self-energy term $\Sigma(\varepsilon)$. The self-energy term $\Sigma(\varepsilon)$ can be obtained through iterative calculation of the Green's function [26]. Specifically, for the i -th layer, the self-energy is defined as $\Sigma_i(\varepsilon) = D^\dagger g_{i+1,i+1}(\varepsilon) D$, where $g_{i+1,i+1}(\varepsilon) = 1/(\varepsilon - H_{lay} - \Sigma_{i+1}(\varepsilon))$ represents the surface Green's function for the $i+1$ th layer, and ε denotes energy. Since the gap closing occurs at $\varepsilon = 0$, we consider $\Sigma(\varepsilon = 0)$ due to its effective description of physics around $\varepsilon = 0$.

We calculated the local Chern markers $C_z(l)$ under varying surface magnetization M_A [Fig. 3(b)]. The computation re-

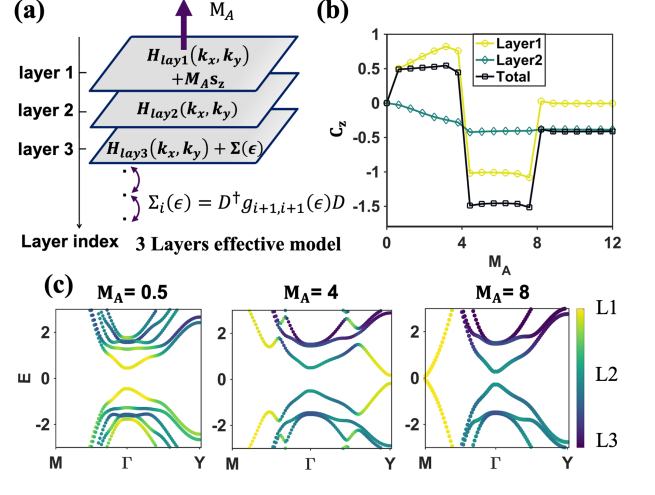


Figure 3. (a) Schematic diagram of the three-layer effective model. Ellipses indicate the process of self-energy iteration. (b) $C_z(1)$, $C_z(2)$, and C_z as a function of M_A . (c) Band structures under different M_A with colors indicating the layer of the states.

sults reveal a transition of the surface Chern number \mathbb{C}_z from $\frac{1}{2}$ to $-\frac{3}{2}$ to $-\frac{1}{2}$ [black line in Fig. 3(b)], coinciding with the numerical results shown in Fig. 1(b). It is noteworthy that, before the first gap closing (at X, Y points), as M_A increases, the local Chern marker of the first layer gradually increases from $\frac{1}{2}$ to 1, while that of the second layer decreases from 0. Although there is a redistribution of $C_z(l)$, the total Chern number of the three-layer system, i.e. surface Chern number \mathbb{C}_z , remains at $1/2$. This redistribution of $C_z(l)$ can be detected through measurements of the ME coefficient, in Sec. V, we will provide a detailed discussion of this. Fig. 3(c) displays the band structures and layer-resolved projections under different M_A . At $M_A = 0.5$, the color of the Dirac cone at Γ point is yellow, indicating that the wave function is predominantly distributed in the first layer. The presence of a gapped Dirac cone on the first layer corresponds to $C_z(1) \approx \frac{1}{2}$ at $M_A = 0.5$ [Fig. 3(b)]. However, with the increase of M_A , the structure of the Dirac cone gradually disappears, which corresponds with the redistribution of $C_z(l)$ between the first layer and the second layer. After the gap closing and reopening at the X/Y point, a Dirac cone structure reemerges in the second layer, marked by green in the band structure [Fig. 3(c) with $M_A = 4$]. The reappearance of the Dirac cone in the second layer results in $C_z(2)$ approaching $-\frac{1}{2}$ [see Fig. 3(b)], indicating that the topological transition in the first layer leads to the reformation of topological surface states in the second layer and $\mathbb{C}_z \approx -\frac{3}{2}$. With the furthermore increase of M_A , as the band closes and reopens at the M point, the local Chern marker of the first layer becomes zero, signifying the transition of the first layer to the FMI phase and \mathbb{C}_z jumping to $-\frac{1}{2}$. The detailed evolutions of energy bands with changing magnetization can be found in the Fig. 6 of Appendix A.

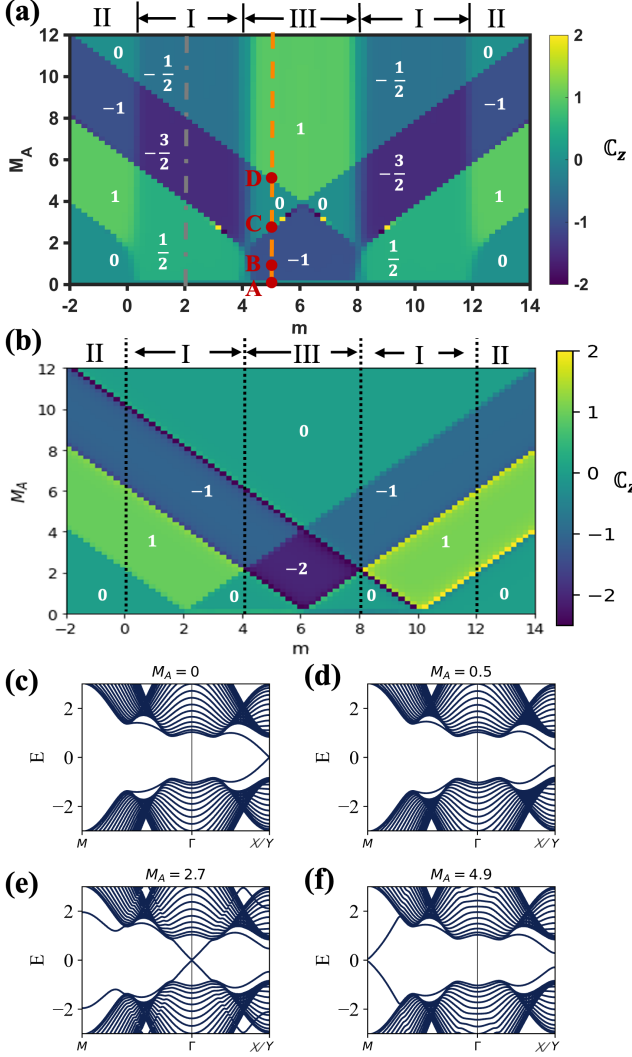


Figure 4. (a) Surface Chern number \mathbb{C}_z versus the surface magnetization M_A and the mass term m . Fig. 1(b) corresponds to the gray dash-dotted line in (a). (b) \mathbb{C}_z of the single-layer model changes in response to alterations in M_A and m . (c-f) These figures respectively correspond to the band structures at points A-D, which are identified with red markers in (a).

IV. PHASE DIAGRAM OF 3D TI WITH SURFACE MAGNETIZATION

Next, we investigate how the surface Chern number \mathbb{C}_z is affected by the topology of the bulk which is defined by the topological mass term m [27]. Fig. 4(a) shows \mathbb{C}_z with respect to both the surface magnetization M_A and the mass term m . The transition of \mathbb{C}_z from $\frac{1}{2}$ to $-\frac{3}{2}$ to $-\frac{1}{2}$ can only be observed in the topologically nontrivial bulk region (interval I), i.e., $0 < m < 4B$ and $8B < m < 12B$ [17]. In the topologically trivial bulk regions (II, III), the behavior of \mathbb{C}_z with respect to changes in M_A is inconsistent. In the region II where $m < 0$ and $m > 12B$, as M_A increases, \mathbb{C}_z changes from $0 \rightarrow 1 \rightarrow -1 \rightarrow 0$. In the region III ($4B < m < 8B$), as M_A

increases, the surface Chern number \mathbb{C}_z exhibits a transition of $-1 \rightarrow 0 \rightarrow 1$. We attribute the distinct behavior of \mathbb{C}_z in regions II and III to different Z_4 topological classification [13, 17, 28].

To provide an explanation for the differing behavior of surface Chern number \mathbb{C}_z in the regions II and III under the influence of surface magnetization M_A , we calculated the phase diagram as a function of the magnetization M_A and topological mass m for the single-layer system (See Fig. 4(b)). This diagram reflects surface phase transitions under magnetization conditions without bulk effects. In region II, the variation of \mathbb{C}_z in the single-layer system matches that of the multi-layer system, implying that \mathbb{C}_z of the multi-layer system remains unaffected by bulk influence.

Conversely, in the topologically trivial region III, changes in surface magnetization M_A result in different behaviors in the surface Chern number \mathbb{C}_z between the single-layer and multi-layer systems. In this case, \mathbb{C}_z undergoes a transition from $0 \rightarrow -2 \rightarrow -1 \rightarrow 0$ in the single-layer system [see Fig. 4(b)], but \mathbb{C}_z changes from $-1 \rightarrow 0 \rightarrow 1$ in the multi-layer system [see Fig. 4(a)], indicating the impact of the bulk within the region III. Specifically, at $M_A = 0$, the multi-layer model exhibits two Dirac cones at the X/Y points due to the bulk presence [see Fig. 4(c)]. However, a single-layer system lacks these Dirac cones. When the surface magnetization M_A is small, the two Dirac cones open up gaps [Fig. 4(d)], each contributing $-1/2$ to surface Chern number \mathbb{C}_z . Consequently, \mathbb{C}_z of the multi-layer system under small M_A is -1 . As the surface magnetization M_A increases, \mathbb{C}_z of the multi-layer system in the region III transitions from -1 to 0 . The physics picture here is similar to the surface Chern number \mathbb{C}_z transition from $1/2$ to $-3/2$ in the region I, i.e., the topological transition of the first layer and the reformation of Dirac cone in the second layer. In particular, accompanied by the non-adiabatic change of the first layer (gap closing and reopening at Γ point, see Fig. 4(e)), the first layer enters the QAH phase with $\mathbb{C}_z = -1$, and simultaneously, the Dirac cone at the X/Y point re-forms in the second layer. Furthermore, the effective magnetization direction on the second layer is opposite to that of the first layer, leading to gap opening and contributing to $+1$ surface Chern number \mathbb{C}_z . Therefore, \mathbb{C}_z of the multi-layer system results from the QAH of the first layer and the newly formed gapped Dirac cones in the second layer, yielding a total surface Chern number of $-1 + 1 = 0$. Similarly, with further increases in M_A , the first layer undergoes another non-adiabatic change (gap closing and reopening at M point, see Fig. 4(f)), transitioning to a zero Chern number in the FMI phase. Consequently, the overall surface Chern number \mathbb{C}_z of the multi-layer system is contributed by the second layer, resulting in $+1$.

In summary, both region II and region III fall under the topological trivial phase ($v_0 = 0$) according to Z_2 topological classification. However, their Z_4 topological numbers are distinct [13, 28]. For the region II, $Z_4 = (0; 0, 0, 0)$, and for the region III, $Z_4 = (0; 1, 1, 1)$, which corresponds to the presence of an even number of Dirac cones on the surface of the region III [17]. Consequently, we attribute the contrasting behavior of surface Chern numbers under surface magnetization

variations between the region II and region III to their distinct Z_4 topological classifications.

V. TOPOLOGICAL ME EFFECT AND SIX TERMINAL HALL TRANSPORT

The discontinuous platform transition of the surface Chern number \mathbb{C}_z , driven by variations in surface magnetization M_A , can be experimentally detected by measuring the ME response coefficient α_{zz} [29, 30]. It's worth noting that, to detect the ME effect, we apply outward-pointing magnetization M_A on the lateral surface of a 3D TI in the subsequent calculations, as depicted in Fig. 5(a). Upon applying an electric field E_z in the z -direction, the lateral surface will trigger a Hall current $j_H = \sigma_H E_z$, where σ_H represents the surface Hall conductance [as shown in Fig. 5(a)]. According to Ampere's law, the magnetization along the z -direction is defined as $M_z = j_H/c$, where c is the speed of light. As the ME response coefficient satisfies the relation $M_z = \alpha_{zz} E_z$, the ME coefficient and the lateral surface Hall conductance differ by only a constant c [10]. Consequently, we expect that with an increase in lateral surface magnetization M_A , the system's ME response coefficient will exhibit a transition from $\frac{1}{2}$ to $-\frac{3}{2}$ and then to $-\frac{1}{2}$, as shown by the red dashed line in Fig. 5(b). To evaluate the ME effect, we employ linear response theory to compute the orbital magnetization generated by a vertically applied electric field E_z (see Appendix C). By constructing a square in the xy -plane with a side length of L sites while maintaining translation symmetry along the z direction, we obtain the ME response coefficient α_{zz} via the Kubo formula [6, 31]. The numerical results for the α_{zz} with different side length L are illustrated in Fig. 5(b). As the α_{zz} only converges when L tends to infinity [22], increasing L progressively brings the numerical α_{zz} closer to theoretical values. Additionally, we derive the ME response coefficient α_{zz} at the thermodynamic limit ($L \rightarrow \infty$) through fitting (see Appendix C), and the fitting results shows agreement with the theoretical outcomes [see Fig. 5(b)].

As discussed in Sec. III [refer to Fig. 3(b)], we have observed that for $M_A < 4$, an increase in magnetization M_A leads to a redistribution of local Chern markers across multiple layers of the surface. However, since the overall surface Chern number remains constant, this redistribution of local Chern markers may not be detectable through conventional transport experiments. However, we emphasize that the changes in the distribution of local Chern markers can be experimentally observed by measuring the ME response coefficient during variations in the lateral surface magnetization [as shown in Fig. 5(a)]. Specifically, in finite-sized systems where $M_A < 4$, as the lateral surface magnetization increases, the ME response coefficient gradually rises [see Fig. 5(b)]. This can be attributed to the distinct cyclotron radii of the current in the outermost and second outermost layers. Consequently, this leads to different weights in the contributions of the outermost and second outermost layers to the z -direction magnetization. In experiments, this phenomenon can be observed by measuring the change in magnetic flux along the z -

direction using a Superconducting Quantum Interference Device (SQUID).

The variation of the surface Chern number \mathbb{C}_z with the surface magnetization M_A can also be observed through distinctive Hall conductance plateau transitions in a six-terminal system. Let's consider a 3D TI slab under open boundary conditions with the sizes $L_z = 15$, $L_y = 20$ and $L_x = 100$ [Fig. 5(c)]. We assume a magnetic field applied along the z direction, corresponding to a magnetic flux of $\phi = \pm 0.1$ per unit cell. The surface magnetization M_A is applied to the lateral surfaces (but we still use \mathbb{C}_z to describe the surface Chern number of the lateral surface). Employing a six-terminal Hall bar structure as depicted in Fig. 5(c), we calculate the Hall conductance using the Landauer-Büttiker formula [26, 32–35](see Appendix D). Fig. 5(d) illustrates how the upper surface Hall conductance changes with varying lateral surface magnetization M_A for $\phi = \pm 0.1$. When $\phi = 0.1$, the magnetic field leads to $\mathbb{C}_\phi = \frac{1}{2}$ on the upper surface [13]. As M_A increases, a transition of surface Chern numbers \mathbb{C}_z occurs on the lateral surface, transitioning from $\frac{1}{2}$ to $-\frac{3}{2}$ finally to $-\frac{1}{2}$. The difference between \mathbb{C}_ϕ and \mathbb{C}_z results in a domain wall between the lateral and upper surfaces, leading to the chiral modes appearing at the boundary of the upper surface, with the number of the chiral modes $n = \mathbb{C}_z - \mathbb{C}_\phi$. The Hall conductance of the upper surface corresponds to the number of chiral modes, i.e., $\sigma_{xy} = n \frac{e^2}{h}$. Therefore, with the increasing M_A , the Hall conductance undergoes a transition from 0 to $-2 \frac{e^2}{h}$ to $-\frac{e^2}{h}$ [see the purple line in Fig. 5(d)]. When $\phi = -0.1$, the Chern number on the upper surface is $-\frac{1}{2}$. Similarly, with the increasing magnetization, the Hall conductance undergoes a transition from $\frac{e^2}{h}$ to $-\frac{e^2}{h}$ to 0, as depicted by the purple line in Fig. 5(d).

VI. DISCUSSION AND CONCLUSION

To investigate the possibility of realizing the topological phase transition mentioned in the paper using existing materials, calculations were performed based on the real parameters of the material Bi_2Se_3 in Appendix E. However, the results indicate that the surface magnetic gap required for the phase transition is slightly larger than what can currently be achieved experimentally. In order to experimentally observe the surface phase transition of 3D TI, it is required to minimize the material band width and maximize the Zeeman splitting induced by the surface magnetization as much as possible. Considering these requirements, 3D d-orbital TIs are ideal candidates for realizing the aforementioned phase transition. In such materials, the radial wave functions of the d orbitals are predominantly distributed near the atomic nucleus, leading to reduced overlap integrals and narrower band widths. Additionally, the Zeeman splitting effect of the d orbitals is relatively strong. A recent first-principles calculations suggest that materials within the antiferroite Cu_2S family can achieve d-orbital strong 3D TI phase [36]. Furthermore, Z_2 strong TIs with flat band structures are also an ideal choice for realizing such phase transitions due to the small band width

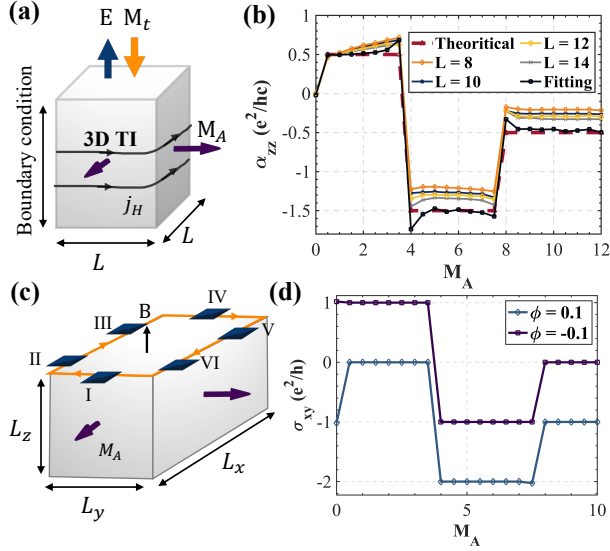


Figure 5. (a) Sketch of a 3D TI with surface magnetization M_A normal to the side surfaces (purple arrows). With the application of an electric field \mathbf{E} , the surface Hall effect induces a circulating current denoted as j_H , consequently giving rise to a bulk magnetization $M_t \parallel \mathbf{E}$. (b) ME coefficient α_{zz} as a function of M_A with different side length L . (c) Illustration of a Hall bar device constructed using a 3D TI, featuring metallic leads attached to the upper surface (highlighted in blue). The upper surface displays the chiral edge channels, as denoted by the orange curve. In this context, the magnetic field along the z -direction and the magnetization on the lateral surface are represented by black and purple arrows, respectively. (d) Hall conductance on the upper surface as the function of the side surface magnetization M_A with Fermi energy $E_F = 0.1$.

[37]. Meanwhile, quantum simulation techniques have undergone significant advancements in recent years, and many condensed matter systems have achieved success through this approach [38–45]. Notably, Wilson lattice Hamiltonians, identical in form to the model used in this paper, have been realized in circuit systems [46]. Therefore, quantum simulation methods also provide a powerful avenue for investigating such surface phase transitions.

In summary, our study unveils a surface phase transition with broken bulk-boundary correspondence in 3D TIs induced by surface magnetization. Employing both a realistic lattice model and a three-layer effective model, we calculate the surface Chern number. Remarkably, as surface magnetization increases, the surface Chern number exhibits the transition from $\frac{1}{2}$ to $-\frac{3}{2}$ and finally to $-\frac{1}{2}$, which cannot be explained by low-energy theories. We attribute these transitions to the evolution of the first-layer massive Dirac fermions into quantum QAH and FMI phases, and the reemergence of a second-layer massive Dirac fermion with opposite mass sign. These topological transitions also lead to the sudden jumps in the ME coefficient and the Hall conductance, which can experimentally be observed. Our investigation reveals a new phase with broken bulk-boundary correspondence, enriching understandings of the properties of TIs.

VII. ACKNOWLEDGMENT

Y.-H. W. is grateful to Jiayu Li, Ming Gong, Zhihao Huang and Ludan Zhang for fruitful discussions. This work was financially supported by the National Natural Science Foundation of China (Grant No. 12374034 and No. 11921005), the Innovation Program for Quantum Science and Technology (2021ZD0302403), and the Strategic priority Research Program of Chinese Academy of Sciences (Grant No. XDB28000000). We also acknowledge the Highperformance Computing Platform of Peking University for providing computational resources.

Appendix A: Evolution of Band Structure with Surface magnetization Variation

In this section, we will present a more detailed variation of the system's band structure with increasing surface magnetization M_A . The model and computational methods used are consistent with those in the main text. When the surface magnetization $M_A = 0$, bulk-boundary correspondence ensures the existence of gapless Dirac cones on the surface of the 3D TI (see Fig. 6 with $M_A = 0$). Upon introducing a small M_A , the breaking of TRS on the surface leads to the gapped Dirac cone (Fig. 6 with $M_A = 0.5$) and the surface Chern number \mathbb{C}_z of $1/2$ (Fig. 1(b)). Alongside the band closing and reopening at the XY points (Fig. 6 with $M_A = 3.8$), the first layer undergoes a topological phase transition, resulting in a jump of \mathbb{C}_z from $1/2$ to $-3/2$. With further increase in magnetization M_A , the band at the M point experiences a similar closing and reopening (See Fig. 6 with $M_A = 7.9$), causing \mathbb{C}_z to sharply shift from $-3/2$ to $-1/2$. From the projection of wave functions, we can observe that the $-1/2$ surface Chern number \mathbb{C}_z is contributed by the massive Dirac fermion in the second layer (See Fig. 6 with $M_A = 10$).

Appendix B: Effective magnetization on second layer

In our model, the magnetization M_A is added on the first layer (the outermost layer), and the magnetization term is represented as $M_A \sigma_0 s_z$. However, an effective magnetization in the second layer can be induced by the magnetization M_A in the first layer. The induced effective magnetization in the second layer can be obtained by calculating the self-energy correction $\Sigma_{mag}(\varepsilon)$ of the first layer's magnetization with respect to the second layer [26],

$$\Sigma_{mag}(\varepsilon) = D^\dagger \frac{1}{\varepsilon - M_A s_z + i\eta} D,$$

where η is an infinitesimally small quantity approaching 0 and $D = \frac{A}{2i} \sigma_x s_z + B \sigma_z s_0$ is the interlayer hopping with $A = 1$ and $B = 1$. The symbol ε represents energy. Similar to the main text, here we adopt the approximation $\varepsilon = 0$, then the self-energy correction reduces into:

$$\Sigma_{mag}(0) = -\frac{5}{4M_A} \sigma_0 s_z + \frac{1}{M_A} \sigma_y s_0$$

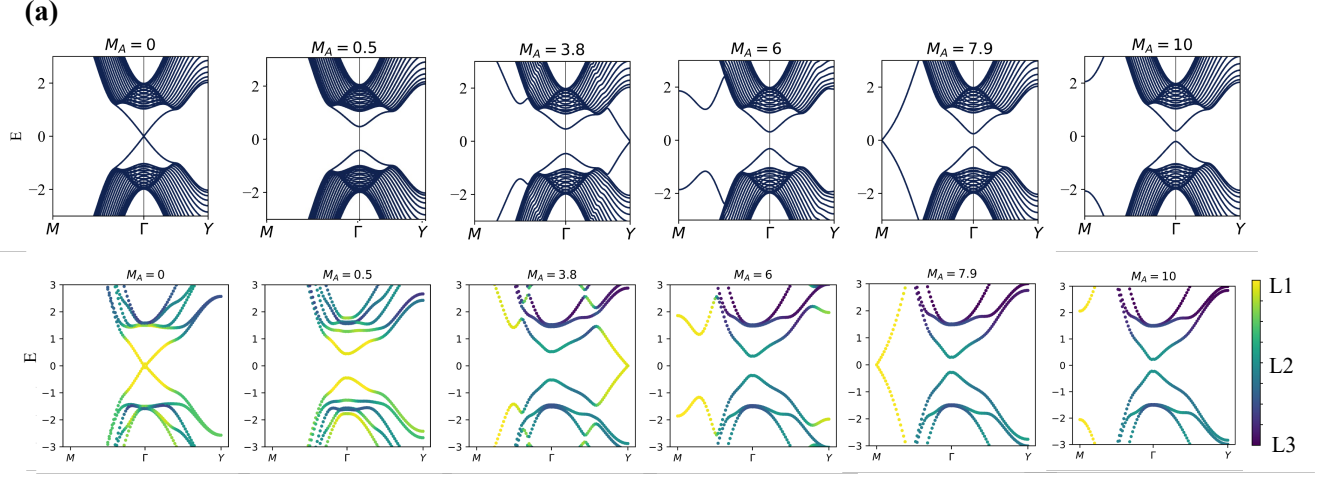


Figure 6. (a) Band structure of systems under different surface magnetizations M_A (corresponding to the red points in Fig. 1(b)). Upper part: Band structure calculations for a 20-layer slab model. Lower part: Band structure calculations for a 3-layer effective model, where colors denote the state's corresponding layer. The first, second, and third layers are respectively denoted by yellow, green, and purple.

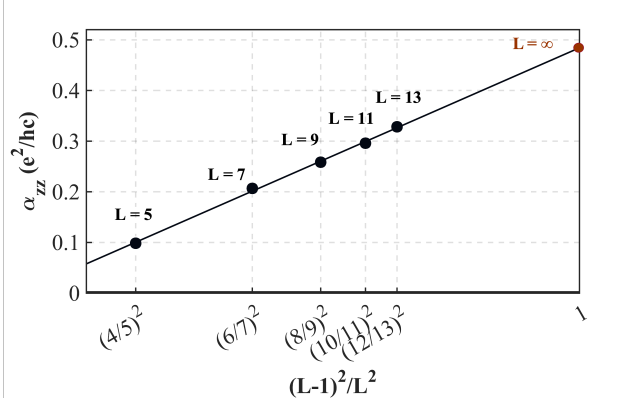


Figure 7. (a) A representative diagram illustrates the ME coupling coefficient, α_{zz} , for systems with different side lengths L . The ME coefficient in the thermodynamic limit ($L \rightarrow \infty$) is marked by the red data point on the graph. The surface magnetization $M_A = 10.5$ in this plot.

The first term corresponds to the effective magnetization of the second layer, with its sign opposite to that of the first layer.

Appendix C: Calculation and fitting of magneto-electric coupling coefficient

ME response of a bounded sample can be derived by linear response theory [6]:

$$\alpha_{zz} = \sum_{\substack{k_z \\ i \in \text{occ.} \\ j \in \text{unocc.}}} \frac{\hbar \text{Im} \left[\langle k_z, i | \hat{M}_z | k_z, j \rangle \langle k_z, j | \hat{J}_z | k_z, i \rangle \right]}{a N_{k_z} \mathcal{A} (\varepsilon_{i, k_z} - \varepsilon_{j, k_z})^2} \quad (\text{C1})$$

The orbital magnetic moment, denoted as \mathbf{M} , is given by $\widehat{\mathbf{M}} = -(e/2c)\hat{\mathbf{r}} \times \hat{\mathbf{v}}$ [47]. Here, $\hat{\mathbf{r}}$ and $\hat{\mathbf{v}}$ represent the position and velocity operators, and the current density \mathbf{J} is expressed as $\mathbf{J} = e \hat{\mathbf{v}}$. \mathcal{A} represents the cross-sectional area in the xy -direction of the system, while a stands for the lattice constant in the z -direction. Here, $|k_z, i\rangle$ denotes the i -th eigenstate with momentum k_z and corresponding eigenvalue ε_{i, k_z} . In the summation, i and j are limited to occupied and unoccupied bands, respectively.

Magnetization on the lateral surface leads to a redistribution of the local Chern markers between the outermost and second outermost layers, causing z -directional electric fields to induce Hall currents in both layers simultaneously. Due to the diverse angular momentum of Hall ring currents in different layers, variations occur in the electrically induced magnetic moment M , subsequently causing changes in the α_{zz} . The coefficients $\alpha_{zz}^{\text{out/in}}$ are defined as the ME coupling coefficients of the system considering only the magnetic moments generated by the Hall currents in the outermost (second outermost) layer. Since the overall magnetic moment of the system results from the contributions of both the outermost and second outermost layer currents, there exists a correlation between α_{zz} and $\alpha_{zz}^{\text{out}}, \alpha_{zz}^{\text{in}}$.

$$L^2 \alpha_{zz} = L^2 \alpha_{zz}^{\text{out}} + (L-1)^2 \alpha_{zz}^{\text{in}} \quad (\text{C2})$$

α_{zz} converges in the thermodynamic limit ($L \rightarrow \infty$) [22]

$$\begin{aligned} \alpha_{zz} &= \lim_{L \rightarrow \infty} \left[\alpha_{zz}^{\text{out}} + \left(\frac{L-1}{L} \right)^2 \alpha_{zz}^{\text{in}} \right] \\ &= \alpha_{zz}^{\text{out}} + \alpha_{zz}^{\text{in}} \end{aligned}$$

To obtain α_{zz} in the thermodynamic limit, we calculate α_{zz} for different side lengths L , and take $\alpha_{zz}^{\text{out}} + \alpha_{zz}^{\text{in}}$ as the fitting outcome for α_{zz} (see Fig. 7).

Appendix D: Landauer-Büttiker formula

In a Hall-bar configuration like that shown in Fig. 5(c), we can employ the Landauer-Büttiker formula to compute the Hall conductance on the system's surface. The Landauer-Büttiker formula is expressed as:[48, 49]

$$\begin{bmatrix} T_{11} & T_{12} & T_{13} & T_{14} & T_{15} & T_{16} \\ T_{21} & T_{22} & T_{23} & T_{24} & T_{25} & T_{26} \\ T_{31} & T_{32} & T_{33} & T_{34} & T_{35} & T_{36} \\ T_{41} & T_{42} & T_{43} & T_{44} & T_{45} & T_{46} \\ T_{51} & T_{52} & T_{53} & T_{54} & T_{55} & T_{56} \\ T_{61} & T_{62} & T_{63} & T_{64} & T_{65} & T_{66} \end{bmatrix} \times \begin{bmatrix} V_1 \\ V_2 \\ V_3 \\ V_4 \\ V_5 \\ V_6 \end{bmatrix} = \begin{bmatrix} I_1 \\ I_2 \\ I_3 \\ I_4 \\ I_5 \\ I_6 \end{bmatrix} \quad (\text{D1})$$

where $T_p = -\sum_{q(q \neq p)} T_{pq}$. V_p and I_p represent the voltage and current at lead p , respectively. The transmission coefficient from lead q to lead p , denoted as T_{pq} , can be obtained using the formula $T_{pq} = \text{Tr}(\Gamma_p G^R \Gamma_q G^A)$, where $G^{R/A} = (\varepsilon_F - H_D - \sum_{p=1}^6 \Sigma_p^{R/A})^{-1}$ are the retarded and advance Green's functions.[48, 49] $\Gamma_p = i(\Sigma_p^R - \Sigma_p^A)$ is the line width function, with $\Sigma_p^{R/A}$ being the self energy of lead p . [48, 49] Given the current vector as $\vec{I} = [I, 0, 0, -I, 0, 0]$, the voltage at each port can be determined by solving Eq. (D1). The longitudinal resistivity $\rho_{xx} = (V_2 - V_3)/I$ and Hall resistivity $\rho_{xy} = (V_2 - V_6)/I$. Furthermore, the Hall conductance can be computed using $\sigma_{xy} = \rho_{xy}/(\rho_{xx}^2 + \rho_{xy}^2)$. In the calculations, we set the central region's thickness as $L_z = 15$, width as $L_y = 20$, and length as $L_x = 100$. The height and width of the leads are set as 3 and 10, respectively.

Appendix E: Phase transition points under real material parameters

In the paper, we utilize dimensionless parameters to enhance the clarity of the physical picture. To underscore practical relevance, this appendix focuses on utilizing parameters specific to realistic materials.

We compare our approach with the low-energy model of Bi_2Se_3 [50], where the Hamiltonian near the Gamma point is given by

$$H^{3D} = \varepsilon_0(\mathbf{k})s_0\sigma_0 + M(\mathbf{k})s_0\sigma_z + A_1k_zs_z\sigma_x + A_2(k_xs_x + k_ys_y)\sigma_x.$$

Here, $k_\perp = k_x^2 + k_y^2$, $\varepsilon_0(\mathbf{k}) = C + D_1k_z^2 + D_2k_\perp^2$, and $M(k) = M_0 - B_1k_z^2 - B_2k_\perp^2$. In this study, we simplify by setting $\varepsilon_0(k) = 0$, $M_0 = 0.28 \text{ eV}$, $B_1 = B_2 = 0.1 \text{ eV nm}^2$, and $A_1 = A_2 = 0.1 \text{ eV nm}$. The parameters M_0 and B_1 here are consistent with the real material Bi_2Se_3 [50].

Based on this low-energy model within a cubic lattice with a lattice constant of $a = 1 \text{ nm}$ allows us to establish the relation between the parameters of real materials and those in Eq. (1). For realistic parameter of Bi_2Se_3 : $B_1/a^2 = 0.1 \text{ eV}$, it corresponds to the dimensionless parameter $B = 1$ in Eq. (1). Similarly, the topological mass $M_0 = 0.28 \text{ eV}$ corresponds to $m = 2.8$, and $A_1/a = 0.1 \text{ eV}$ corresponds to $A = 1$. Under this parameter mapping, the phase transition induced by the surface magnetization of Bi_2Se_3 can be observed in the phase diagram Fig. 4(a), where the unit 1 corresponds to 0.1 eV for Bi_2Se_3 . With the increase of surface magnetization, the surface magnetic gaps corresponding to two phase transitions are approximately $M_{A1} \approx 0.32 \text{ eV}$ and $M_{A2} \approx 0.72 \text{ eV}$ respectively. However, the intrinsic magnetic topological insulator MnBi_2Te_4 currently exhibits the largest observed surface magnetic gap, measuring more than 60 meV [51, 52]. Therefore, achieving the phase transition discussed in this paper still presents some challenges with the existing materials.

-
- [1] A. Bansil, H. Lin, and T. Das, *Rev. Mod. Phys.* **88**, 021004 (2016).
- [2] M. Z. Hasan and C. L. Kane, *Rev. Mod. Phys.* **82**, 3045 (2010).
- [3] B. A. Bernevig, T. L. Hughes, and S.-C. Zhang, *Science* **314**, 1757 (2006,12,15).
- [4] C. L. Kane and E. J. Mele, *Phys. Rev. Lett.* **95**, 226801 (2005).
- [5] M. König, S. Wiedmann, C. Brüne, A. Roth, H. Buhmann, L. W. Molenkamp, X.-L. Qi, and S.-C. Zhang, *Science* **318**, 766 (2007,11,2).
- [6] Y. Wan, J. Li, and Q. Liu, *Nat. Sci. Rev.*, nwac138 (2022).
- [7] J. Wang, B. Lian, X.-L. Qi, and S.-C. Zhang, *Phys. Rev. B* **92**, 081107 (2015).
- [8] A. M. Essin, J. E. Moore, and D. Vanderbilt, *Phys. Rev. Lett.* **102**, 146805 (2009).
- [9] M. Mogi, Y. Okamura, M. Kawamura, R. Yoshimi, K. Yasuda, A. Tsukazaki, K. S. Takahashi, T. Morimoto, N. Nagaosa, M. Kawasaki, Y. Takahashi, and Y. Tokura, *Nat. Phys.* **18**, 390 (2022).
- [10] A. Sekine and K. Nomura, *Journal of Applied Physics* **129**, 141101 (2021).
- [11] D. M. Neno, C. A. C. Garcia, J. Gooth, C. Felser, and P. Narang, *Nat Rev Phys* **2**, 682 (2020).
- [12] X.-L. Qi, T. L. Hughes, and S.-C. Zhang, *Phys. Rev. B* **78**, 195424 (2008).
- [13] L. Fu and C. L. Kane, *Phys. Rev. B* **76**, 045302 (2007).
- [14] H. Zhou, H. Li, D.-H. Xu, C.-Z. Chen, Q.-F. Sun, and X. C. Xie, *Phys. Rev. Lett.* **129**, 096601 (2022).
- [15] F. Wilczek, *Phys. Rev. Lett.* **58**, 1799 (1987).
- [16] X.-L. Qi and S.-C. Zhang, *Rev. Mod. Phys.* **83**, 1057 (2011).
- [17] S.-Q. Shen, *Topological Insulators: Dirac Equation in Condensed Matters*, Springer Series in Solid-State Sciences, Vol. 174 (Springer Berlin Heidelberg, Berlin, Heidelberg, 2012).
- [18] D. Xiao, J. Jiang, J.-H. Shin, W. Wang, F. Wang, Y.-F. Zhao, C. Liu, W. Wu, M. H. W. Chan, N. Samarth, and C.-Z. Chang, *Phys. Rev. Lett.* **120**, 056801 (2018).
- [19] M. Mogi, M. Kawamura, R. Yoshimi, A. Tsukazaki, Y. Kozuka, N. Shirakawa, K. S. Takahashi, M. Kawasaki, and Y. Tokura,

- Nat. Mater.* **16**, 516 (2017).
- [20] K. Yasuda, M. Mogi, R. Yoshimi, A. Tsukazaki, K. S. Takahashi, M. Kawasaki, F. Kagawa, and Y. Tokura, *Science* **358**, 1311 (2017).
- [21] R. Bianco and R. Resta, *Phys. Rev. B* **84**, 241106 (2011).
- [22] T. Rauch, T. Olsen, D. Vanderbilt, and I. Souza, *Phys. Rev. B* **98**, 115108 (2018).
- [23] N. Varnava and D. Vanderbilt, *Phys. Rev. B* **98**, 245117 (2018).
- [24] M. Gu, J. Li, H. Sun, Y. Zhao, C. Liu, J. Liu, H. Lu, and Q. Liu, *Nat. Commun.* **12**, 3524 (2021).
- [25] G. Schubert, H. Fehske, L. Fritz, and M. Vojta, *Phys. Rev. B* **85**, 201105 (2012).
- [26] S. Datta, *Electronic transport in mesoscopic systems* (Cambridge university press, 1997).
- [27] B. A. Bernevig, *Topological Insulators and Topological Superconductors* (Princeton University Press, Princeton, 2013).
- [28] L. Fu, C. L. Kane, and E. J. Mele, *Phys. Rev. Lett.* **98**, 106803 (2007).
- [29] V. Dziom, A. Shuvaev, A. Pimenov, G. V. Astakhov, C. Ames, K. Bendias, J. Böttcher, G. Tkachov, E. M. Hankiewicz, C. Brüne, H. Buhmann, and L. W. Molenkamp, *Nat. Commun.* **8**, 15197 (2017).
- [30] M. M. Vopson, Y. K. Fetisov, G. Caruntu, and G. Srinivasan, *Materials* **10**, 963 (2017).
- [31] G. D. Mahan, *Many-Particle Physics* (Springer US, Boston, MA, 2000).
- [32] M. Büttiker, *Phys. Rev. B* **38**, 9375 (1988).
- [33] D. S. Fisher and P. A. Lee, *Phys. Rev. B* **23**, 6851 (1981).
- [34] R. Landauer, *Philosophical Magazine* **21**, 863 (1970).
- [35] M. Gong, M. Lu, H. Liu, H. Jiang, Q.-F. Sun, and X. C. Xie, *Phys. Rev. B* **102**, 165425 (2020).
- [36] X.-L. Sheng, Z.-M. Yu, R. Yu, H. Weng, and S. A. Yang, *J. Phys. Chem. Lett.* **8**, 3506 (2017,8,3).
- [37] C. Weeks and M. Franz, *Phys. Rev. B* **85**, 041104 (2012).
- [38] S. Sugawa, F. Salces-Carcoba, A. R. Perry, Y. Yue, and I. B. Spielman, *Science* **360**, 1429 (2018).
- [39] W. Ji, L. Zhang, M. Wang, L. Zhang, Y. Guo, Z. Chai, X. Rong, F. Shi, X.-J. Liu, Y. Wang, and J. Du, *Phys. Rev. Lett.* **125**, 020504 (2020).
- [40] T. Xin, Y. Li, Y.-a. Fan, X. Zhu, Y. Zhang, X. Nie, J. Li, Q. Liu, and D. Lu, *Phys. Rev. Lett.* **125**, 090502 (2020).
- [41] W. Cai, J. Han, F. Mei, Y. Xu, Y. Ma, X. Li, H. Wang, Y. P. Song, Z.-Y. Xue, Z.-q. Yin, S. Jia, and L. Sun, *Phys. Rev. Lett.* **123**, 080501 (2019).
- [42] B. Song, L. Zhang, C. He, T. F. J. Poon, E. Hajiyev, S. Zhang, X.-J. Liu, and G.-B. Jo, *Sci. Adv.* **4**, eaao4748 (2018).
- [43] G. Jotzu, M. Messer, R. Desbuquois, M. Lebrat, T. Uehlinger, D. Greif, and T. Esslinger, *Nature* **515**, 237 (2014).
- [44] Z. Meng, L. Huang, P. Peng, D. Li, L. Chen, Y. Xu, C. Zhang, P. Wang, and J. Zhang, *Phys. Rev. Lett.* **117**, 235304 (2016).
- [45] Z. Wu, L. Zhang, W. Sun, X.-T. Xu, B.-Z. Wang, S.-C. Ji, Y. Deng, S. Chen, X.-J. Liu, and J.-W. Pan, *Science* **354**, 83 (2016).
- [46] H. Yang, L. Song, Y. Cao, and P. Yan, *Commun. Phys.* **6**, 211 (2023).
- [47] D. Vanderbilt, *Berry Phases in Electronic Structure Theory: Electric Polarization, Orbital Magnetization and Topological Insulators* (Cambridge University Press, Cambridge, 2018).
- [48] W. Long, Q.-f. Sun, and J. Wang, *Phys. Rev. Lett.* **101**, 166806 (2008).
- [49] Q.-f. Sun and X. C. Xie, *Phys. Rev. Lett.* **104**, 066805 (2010).
- [50] H. Zhang, C.-X. Liu, X.-L. Qi, X. Dai, Z. Fang, and S.-C. Zhang, *Nat. Phys.* **5**, 438 (2009).
- [51] D. A. Estyunin, I. I. Klimovskikh, A. M. Shikin, E. F. Schwier, M. M. Otrokov, A. Kimura, S. Kumar, S. O. Filnov, Z. S. Aliev, M. B. Babanly, and E. V. Chulkov, *APL Mater.* **8**, 021105 (2020).
- [52] M. M. Otrokov, I. I. Klimovskikh, H. Bentmann, D. Estyunin, A. Zeugner, Z. S. Aliev, S. Gaß, A. U. B. Wolter, A. V. Koroleva, A. M. Shikin, M. Blanco-Rey, M. Hoffmann, I. P. Rusinov, A. Y. Vyazovskaya, S. V. Eremeev, Y. M. Koroteev, V. M. Kuznetsov, F. Freyse, J. Sánchez-Barriga, I. R. Amiraslanov, M. B. Babanly, N. T. Mamedov, N. A. Abdullayev, V. N. Zverev, A. Alfonsov, V. Kataev, B. Büchner, E. F. Schwier, S. Kumar, A. Kimura, L. Petaccia, G. Di Santo, R. C. Vidal, S. Schatz, K. Kibner, M. Ünzelmann, C. H. Min, S. Moser, T. R. F. Peixoto, F. Reinert, A. Ernst, P. M. Echenique, A. Isaeva, and E. V. Chulkov, *Nature* **576**, 416 (2019).